

A NON-PARAMETRIC APPROACH TO CONSTRAIN THE TRANSFER FUNCTION IN REVERBERATION MAPPING

YAN-RONG LI¹, JIAN-MIN WANG^{1,2}, AND JIN-MING BAI^{3,4}

Accepted to The Astrophysical Journal

ABSTRACT

Broad emission lines of active galactic nuclei stem from a spatially extended region (broad-line region; BLR) that are composed of discrete clouds and photoionized by the central ionizing continuum. The temporal behaviors of these emission lines are blurred echoes of the continuum variations (i.e., reverberation mapping; RM) and directly reflect structures and kinematics information of BLRs through the so-called transfer function (also known as velocity-delay map). Based on the previous works of Rybicki & Press and Zu et al., we develop an extended, non-parametric approach to determine the transfer function for RM data, in which the transfer function is expressed as a sum of a family of relatively-displaced Gaussian response functions. As such, arbitrary shapes of transfer functions associated with complicated BLR geometry can be seamlessly included, enabling us to relax the presumption of a specified transfer function frequently adopted in previous studies and to let it be determined by observation data. We formulate our approach in the previously well-established framework that incorporates the statistical modeling of the continuum variations as a damped random walk process and takes into account the long-term secular variations which are irrelevant to RM signals. Application to reverberation mapping data shows fidelity of our approach.

Subject headings: galaxies: active — quasars: general — methods: data analysis — methods: statistical

1. INTRODUCTION

The broad-line regions (BLRs) in active galactic nuclei (AGNs), with sizes of light days to light weeks (Kaspi et al. 2000; Bentz et al. 2013), are too compact to be spatially resolved with the existing telescopes, except in a few cases in which the BLRs are magnified by gravitational lensing (Sluse et al. 2012; Guerras et al. 2013). The reverberation mapping (RM) technique provides a powerful, yet unique way to probe structures and kinematics of BLRs through analyzing the temporal variation patterns of emission lines and ionizing continuum (Blandford & McKee 1982; Peterson 1993). Over the past four decades, RM studies have successfully measured BLR sizes for ~ 60 nearby Seyfert galaxies and quasars (e.g., Bentz et al. 2013; Du et al. 2015). Particularly influential was the discovery that BLR sizes intimately correlate with optical luminosities of (sub-Eddington) AGNs, as expected from simple photoionization theory (e.g., Kaspi et al. 2000, 2005; Bentz et al. 2013; Du et al. 2015). This relationship, in combination with the velocity widths of broad emission lines, opens an economic way for virial mass estimation of supermassive black holes (e.g., Vestergaard & Peterson 2006; Ho & Kim 2015). Meanwhile, velocity-binned RM analysis for several AGNs with high-quality spectroscopic data crudely see signatures for diverse kinematics in BLRs, including radial inflows/outflows and non-radial, virialized Keplerian rotations (Bentz et al. 2009; Denney et al. 2010; Grier et al. 2013b; Peterson 2014; Du et al. 2016).

Notwithstanding these advances, the detailed information for structures and kinematics of BLRs remain largely unknown. The major challenges are from RM datasets reli-

ably inferring the transfer function or velocity-delay map and from which obtaining the structure and kinematic information of BLRs. Traditional cross-correlation analysis (e.g., Bentz et al. 2013) or the previous method using a simple specified transfer function (e.g., Rybicki & Kleyana 1994; Zu et al. 2011, 2016)⁵ yields no more than the characterized BLR sizes.

Great effort has gone into developing more sophisticated methods. There are generally two classes of methods depending on the strategy adopted in solving the integral equation that links the variations of continuum and emission lines in RM. One class relies on directly inverting the integral equation, including early attempts based on the Fourier transform (Blandford & McKee 1982) and regularized linear inversion (RLI) methods (Krolik & Done 1995; Skielboe et al. 2015). The former using the Fourier transform was found to require high-fidelity data and thus has not seen much application (Maoz et al. 1991), whereas the latter seeks to discretize the integral equation and employ a differencing operator to suppress the noise. The downside of this class of methods is that the measurement noises cannot be self-consistently incorporated and thus may be very noise sensitive in some cases. The other class relies on indirectly inferring the “best” transfer function that fits the data by supposing prior limits or models on it. The maximum entropy method (Horne 1994) and BLR dynamical modeling method (Pancoast et al. 2011, 2014a; Li et al. 2013) belong to this class. The maximum entropy method finds “simplest” solutions for the transfer function by maximizing the entropy on the premise of a reasonable fit to the data. It, however, does not allow for straightforward uncertainty estimate and model selection (Horne et al. 2003). The BLR dynamical modeling method presumes a specific, but sufficiently flexible toy model for BLRs and directly infer the model parameters, therefore, the transfer function is only an intermediate product (Pancoast et al. 2011; Li et al. 2013).

⁵ Zu et al. (2011) presumed a top-hat transfer function and developed a software called JAVELIN, available at <http://www.astronomy.ohio-state.edu/~yingzu/codes.html#javelin>

¹ Key Laboratory for Particle Astrophysics, Institute of High Energy Physics, Chinese Academy of Sciences, 19B Yuquan Road, Beijing 100049, China; liyanrong@mail.ihep.ac.cn

² National Astronomical Observatories of China, Chinese Academy of Sciences, 20A Datun Road, Beijing 100020, China

³ Yunnan Observatories, Chinese Academy of Sciences, Kunming 650011, China

⁴ Key Laboratory for the Structure and Evolution of Celestial Objects, Chinese Academy of Sciences, Kunming 650011, China

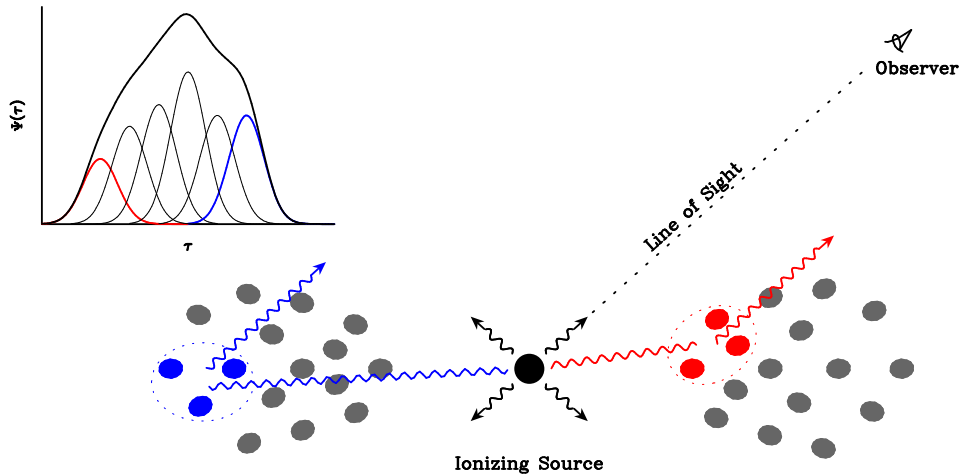


FIG. 1.— Schematic of the transfer function for the system that consists of discrete clouds. The transfer function can be expressed as a sum of many relatively-displaced response functions of local adjacent clouds. For illustrative purposes, the red (blue) curve in the transfer function corresponds to the response from the clouds highlighted in red (blue).

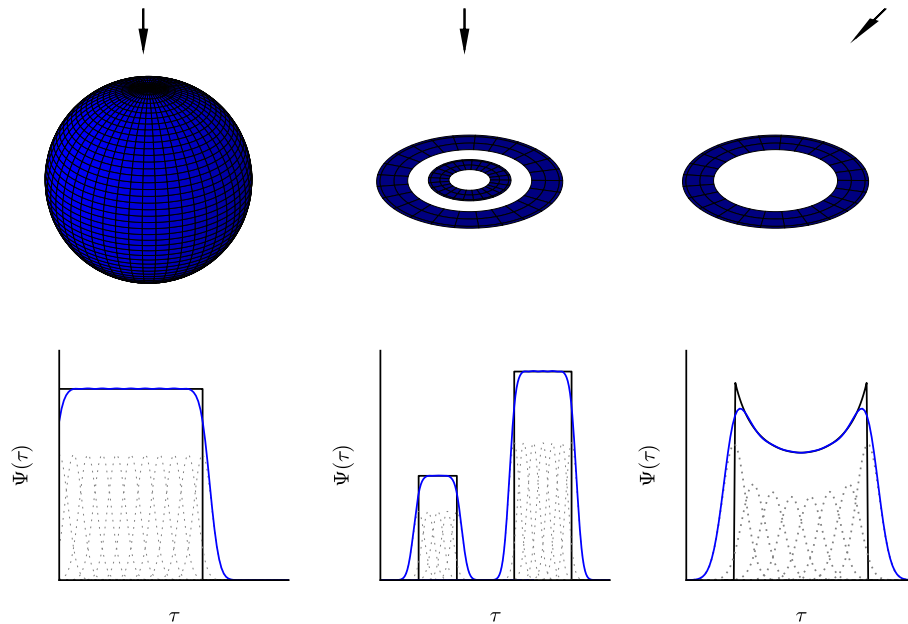


FIG. 2.— Illustrative examples for three types of BLR geometry in which the transfer functions are approximated by a family of Gaussian response functions: (left) a spherical shell, (middle) two disk rings, and (right) an inclined disk ring. Arrows indicate the line of sight. In bottom panels, black lines represent the realistic transfer functions and blue lines represent the sum of the Gaussian functions (grey dotted lines). Our approach can particularly cope with the cases of multimodal or asymmetric transfer functions (e.g., middle panels), in which the previous JAVELIN method may encounter difficulties (see Appendix C).

It cannot yet satisfactorily assess the systematic errors of the adopted model.

In this paper, we describe an extended, non-parametric method to determine the transfer function from RM data, based on the previous works of Rybicki & Press (1992) and Zu et al. (2011). Motivated by the scenario that BLRs are composed of a large number of clouds so that a local adjacent collection of these clouds effectively respond to the central ionizing continuum as a Gaussian response function, we express the transfer function as a sum of a family of relatively displaced Gaussian functions. As such, we can account for arbitrary shapes of the transfer function, therefore, largely relaxing the need of presuming the transfer function

(e.g., Rybicki & Kleyana 1994; Zu et al. 2011) or BLR models (e.g., Pancoast et al. 2011; Li et al. 2013). In this respect our method is model independent and is particularly able to cope with complicated shape of transfer functions (e.g., multimodal) for diverse BLR structures and kinematics.

The paper is organized as follows. We describe the methodology of our approach in detail in Section 2 and perform simulation tests in Section 3. Section 4 presents application to three RM AGNs to illustrate the fidelity of our approach. Discussions and conclusions are given in Section 5. All the time delays quoted in the text are given in the observer’s frame.

2. METHODOLOGY

2.1. The Transfer Function

In RM, variations of broad emission lines $f_l(t)$ are blurred echoes of continuum variations $f_c(t)$ through the transfer function $\Psi(\tau)$ as (Blandford & McKee 1982; Peterson 1993)

$$f_l(t) = \int_{-\infty}^{\infty} \Psi(\tau) f_c(t-\tau) d\tau, \quad (1)$$

where the integral limits are set to account for all possible positively and negatively delayed responses (e.g. Marshall et al. 2008; Shappee et al. 2014). Here, we only show velocity-unresolved RM so that velocity information is not included in the transfer function. However, it is easy to extend our approach to velocity-resolved RM by applying Equation (1) to different velocity bins of emission lines (see below for a discussion). In addition, we also neglect the non-linearity of the response for simplicity (Li et al. 2013). We will provide a way to incorporate non-linear response below.

Mathematically speaking, it is known that an arbitrary function can be expressed as a sum of many slightly-displaced δ -functions, namely, $f(x) = \int f(a)\delta(x-a)da$, where $\delta(x)$ is the Dirac delta function. In practical calculations, one instead uses a set of basic functions with spatial extent to describe a smooth function. A general adoption is Gaussian functions which are often found to be adequate (Sivia & Skilling 2006, p.140). In this spirit, the transfer function in RM is now written as

$$\Psi(\tau) = \sum_{k=1}^K f_k \exp\left[-\frac{(\tau-\tau_k)^2}{2\omega^2}\right], \quad (2)$$

where ω represents the common width of Gaussian responses, τ_k and f_k are the mean lag and weight of k -th response, and K is the number of responses, which can be regarded as a ‘‘smoothing parameter’’. The Gaussian functions are fixed to a common width for the sake of simplicity. Such a choice also helps to relax the parameter degeneracy and improve the computational efficiency of Bayesian inference described below.

The physical interpretation for a such expression is straightforward. The system (i.e., BLRs) under consideration is composed of a large number of clouds. Each cloud responds to the variation of the central source as a δ -response function. A collection of these local adjacent clouds effectively produce a Gaussian response function with a width. This is similar to the principle of local optimally emitting cloud model, widely applied in photon-ionization calculations (Baldwin et al. 1995). Figure 1 shows a schematic illustration of the transfer function of BLRs. In Figure 2, we show examples for three types of BLR geometry: a spherical shell, double disk rings, and an inclined disk ring, in which the transfer function is approximated by a family of Gaussian functions. In particular, there is evidence that H β BLRs have two distinct components (e.g., Brotherton 1996; Sulentic et al. 2000; Hu et al. 2008, 2012 and references therein), indicating that their transfer functions may be bimodal as illustrated in the middle panels of Figure 2.

2.2. Bayesian Inference

With Equation (2), we can directly use the framework developed by Rybicki & Press (1992) and Zu et al. (2011) to infer the best transfer function. We stress that all the formulae presented in this section had been well established by Zu et al. (2011). We list them below for the sake of completeness.

The continuum variation can be well described by a damped random walk (DRW) process (e.g., Kelly et al. 2009, 2014;

Zu et al. 2011; Li et al. 2013). A DRW process is a stationary process so that its covariance function at any two times t_i and t_j only depends on the time difference $\Delta t = t_i - t_j$, which can be simply prescribed as

$$S_{cc}(\Delta t) = \langle f_c(t_i) f_c(t_j) \rangle = \sigma_d^2 \exp\left(-\frac{|\Delta t|}{\tau_d}\right), \quad (3)$$

where angle brackets represent statistical ensemble average, $f_c(t)$ is the continuum driven by the DRW process, τ_d represents the typical damping timescale, and σ_d represents the standard deviation of the process on long timescale ($\gg \tau_d$). On short timescale, the variation amplitude of the process is $\sigma_d \sqrt{2t/\tau_d}$. Combining with Equation (1), the covariance between the line and the continuum is written

$$S_{lc}(\Delta t) = \langle f_l(t_i) f_c(t_j) \rangle = \int_{-\infty}^{\infty} \Psi(\tau) S_{cc}(\Delta t - \tau) d\tau, \quad (4)$$

and the covariance of the line is

$$\begin{aligned} S_{ll}(\Delta t) &= \langle f_l(t_i) f_l(t_j) \rangle \\ &= \int_{-\infty}^{\infty} \int_{-\infty}^{\infty} \Psi(\tau) \Psi(\tau') S_{cc}[\Delta t - (\tau - \tau')] d\tau d\tau'. \end{aligned} \quad (5)$$

In Appendices A and B, we present a detailed derivation for the analytical expressions of these covariances in terms of error function.

The Bayesian posterior probability is obtained as follows (see Rybicki & Press 1992 and Zu et al. 2011 for a thorough derivation). Let \mathbf{y} be a column vector comprised of both the light curves of continuum and line. A set of measurements in a campaign is equal to a realization of some underlying signals with measurement noises as

$$\mathbf{y} = \mathbf{s} + \mathbf{L}\mathbf{q} + \mathbf{n}, \quad (6)$$

where \mathbf{s} is signal of the variations, of which the portion for continuum is described by a DRW process, and \mathbf{n} is the measurement noises. Here the term $\mathbf{L}\mathbf{q}$ is usually used to model general linearly varying trends with time in the light curves (Rybicki & Press 1992), where \mathbf{L} is a matrix of known coefficients and \mathbf{q} is a column vector of unknown linear fitting parameters. For example, to remove separate means of the light curves with a total of $N+M$ measurements, one just configure \mathbf{L} to be a $2 \times (N+M)$ matrix, where N and M are the number of measurements for the continuum and emission line, respectively. The matrix \mathbf{L} has entries of (1,0) for the continuum data points and (0,1) for the line data points (Rybicki & Press 1992; Zu et al. 2013). If one desires to detrend the light curves with long-term secular variations using one-order polynomials, one needs to configure \mathbf{L} to be a $4 \times (N+M)$ matrix (see below for details). Unless stated otherwise, we remove the means of light curves by default in following calculations.

The signal \mathbf{s} and noise \mathbf{n} are assumed to be Gaussian and independent so that their probabilities are simply written as

$$P(\mathbf{s}) \propto \frac{1}{\sqrt{|\mathbf{S}|}} \exp\left(-\frac{\mathbf{s}^T \mathbf{S}^{-1} \mathbf{s}}{2}\right), \quad (7)$$

and

$$P(\mathbf{n}) \propto \frac{1}{\sqrt{|\mathbf{N}|}} \exp\left(-\frac{\mathbf{n}^T \mathbf{N}^{-1} \mathbf{n}}{2}\right), \quad (8)$$

respectively, where $\mathbf{S} = \langle \mathbf{s}\mathbf{s} \rangle$ is the covariance matrix of \mathbf{s} given by Equations (3)-(5), and $\mathbf{N} = \langle \mathbf{n}\mathbf{n} \rangle$ is the covariance matrix of

n . There is no prior information for the linear fitting parameters \mathbf{q} and we assign it a uniform prior probability. Now the probability for a realization \mathbf{y} is

$$P(\mathbf{y}|\sigma, \tau_d, \boldsymbol{\theta}) \propto \iiint P(\mathbf{s})P(\mathbf{n})\delta[\mathbf{y}-(\mathbf{s}+\mathbf{n}+\mathbf{L}\mathbf{q})]d\mathbf{s}d\mathbf{n}d\mathbf{q}, \quad (9)$$

where $\boldsymbol{\theta}$ represents the parameters set for transfer function in Equation (2) and the probability $P(\mathbf{q})$ is uniform so that it is neglected in the above integral. With some mathematical implementation, it can be shown that (Zu et al. 2011)

$$P(\mathbf{y}|\sigma, \tau_d, \boldsymbol{\theta}) = \frac{1}{\sqrt{|\mathbf{C}||\mathbf{L}^T\mathbf{C}^{-1}\mathbf{L}|}} \exp\left(-\frac{\mathbf{y}^T\mathbf{C}_{\perp}^{-1}\mathbf{y}}{2}\right), \quad (10)$$

where $\mathbf{C} = \mathbf{S} + \mathbf{N}$ and $\mathbf{C}_{\perp}^{-1} = \mathbf{C}^{-1} - \mathbf{C}^{-1}\mathbf{L}(\mathbf{L}^T\mathbf{C}^{-1}\mathbf{L})^{-1}\mathbf{L}^T\mathbf{C}^{-1}$. The best estimate for \mathbf{s} is (Rybicki & Press 1992)

$$\hat{\mathbf{s}} = \mathbf{S}\mathbf{C}^{-1}(\mathbf{y} - \mathbf{L}\hat{\mathbf{q}}), \quad (11)$$

and for the linear fitting parameter

$$\hat{\mathbf{q}} = (\mathbf{L}^T\mathbf{C}^{-1}\mathbf{L})^{-1}\mathbf{L}^T\mathbf{C}^{-1}\mathbf{y}. \quad (12)$$

The corresponding variance of the best estimate is, respectively,

$$\langle \Delta \mathbf{s}^2 \rangle = \mathbf{S} - \mathbf{S}\mathbf{C}_{\perp}^{-1}\mathbf{S}, \quad (13)$$

and

$$\langle \Delta \mathbf{q}^2 \rangle = (\mathbf{L}^T\mathbf{C}^{-1}\mathbf{L})^{-1}. \quad (14)$$

The best estimate for the light curves is

$$\hat{\mathbf{y}} = \hat{\mathbf{s}} + \mathbf{L}\hat{\mathbf{q}}, \quad (15)$$

and the corresponding variance is

$$\langle \Delta \mathbf{y}^2 \rangle = \mathbf{S} - \mathbf{S}\mathbf{C}^{-1}\mathbf{S} + (\mathbf{S}\mathbf{C}^{-1}\mathbf{L} - \mathbf{L})(\mathbf{L}^T\mathbf{C}^{-1}\mathbf{L})^{-1}(\mathbf{S}\mathbf{C}^{-1}\mathbf{L} - \mathbf{L})^T. \quad (16)$$

Note that Equations (11), (12), and (15) also provide a way to estimate the value of the light curves at some specified time that may not be one of the already measured points.

According to the Bayes' theorem, the posterior probability distribution for the free parameter set is given by

$$P(\sigma, \tau_d, \boldsymbol{\theta}|\mathbf{y}) = \frac{P(\sigma, \tau_d, \boldsymbol{\theta})P(\mathbf{y}|\sigma, \tau_d, \boldsymbol{\theta})}{P(\mathbf{y})}, \quad (17)$$

where $P(\mathbf{y})$ is the marginal likelihood that serves as a normalization factor to the posterior probability and $P(\sigma, \tau_d, \boldsymbol{\theta})$ is the prior probability for the parameters. We maximize this posterior distribution to obtain the best estimate for the free parameters using a Markov-Chain Monte Carlo (MCMC) method as described in next section.

Long-term secular variability is incidentally detected over the duration of the campaign in some RM objects (e.g., Denney et al. 2010; Li et al. 2013; Peterson et al. 2014). Such long-term trends are uncorrelated with reverberation variations and may bias the reverberation analysis (Welsh 1999). The linear fitting parameter \mathbf{q} provides a natural way to remove such trends. If the long-term trends vary linearly with time ($q_1 + q_2t$), the matrix \mathbf{L} has a form of (Rybicki & Press

1992; Zu et al. 2011)

$$\mathbf{L} = \begin{bmatrix} 1 & t_1^c & 0 & 0 \\ \vdots & \vdots & \vdots & \vdots \\ 0 & t_N^c & 0 & 0 \\ 0 & 0 & 1 & t_1^l \\ \vdots & \vdots & \vdots & \vdots \\ 0 & 0 & 1 & t_M^l \end{bmatrix}, \quad (18)$$

where t_i^c is the i -th time of the N measurement points of the continuum and t_i^l of the M measurement points of the line. In this case, \mathbf{q} is a column vector with four entries, which, respectively, represent the coefficients of the linear trends for the continuum and line data. For the long-term trends with high-order polynomial variation, one can similarly write out the matrix \mathbf{L} by just adding extra columns. In our calculations, when the light curves of the emission line and the driven continuum visually show different long-term trends, we switch on the detrending procedure by assuming the trends vary linearly with time (see below for application to the RM data of Mrk 817).

2.3. Markov Chain Monte Carlo Implementation

The parameters in our approach include: two parameters (σ and τ_d) pertaining to the DRW process in Equation (3); $2K+1$ parameters (f_k s, τ_k s, and ω) to the transfer function in Equation (2). To relax parameter degeneracy, we introduce following simplifications.

- The central lags τ_k of Gaussian responses is assigned by a uniformly spaced grid of time lag over a range of interests, whereas the amplitude f_k is free to be determined. Specifically, we set $\tau_k = \tau_1 + (k-1)\Delta\tau$ for $1 \leq k \leq K$, where $\Delta\tau$ is the grid space, and (τ_1, τ_K) is the range of time lag. Given with the range of time lag, the value of $\Delta\tau$ is determined by the number (K) of Gaussian functions, i.e., $\Delta\tau = (\tau_K - \tau_1)/(K-1)$. The degree of freedom is now reduced to $K+3$.
- The width of Gaussian responses ω is limited by two facts. If ω is too small, unnecessary structures in transfer function will become admissible and hence the reconstructed light curves will appear to be unrealistically noisy; if ω is too large (e.g., $\omega > \Delta\tau$), the neighboring Gaussian responses are indeed indistinguishable. In practice, we found it is adequate to adopt a prior limit of $\omega \sim (\Delta\tau/2, \Delta\tau)$.

The prior probability $P(\sigma, \tau_d, \boldsymbol{\theta})$ in Equation (17) is assigned by assuming that all the free parameters are independent with each other. The Gaussian width has a uniform prior and the rest parameters have a logarithmic prior, which is a usual choice for "scale" parameters that involve a wide range of values (e.g., Sivia & Skilling 2006, p. 108).

At last, we need to choose the number of Gaussian response functions. Strictly speaking, one should employ the Bayesian model selection to choose the best parameter K , i.e., the one that maximizes the probability $P(K|\mathbf{y})$. However, it is very computationally expensive to calculate $P(K|\mathbf{y})$ since one needs to marginalize all the other free parameters. Therefore, we resort to the relatively more economic "non-Bayesian" approaches based on the maximum-likelihood estimate of the parameters (e.g., Hooten & Hobbs 2015). We use the Akaike

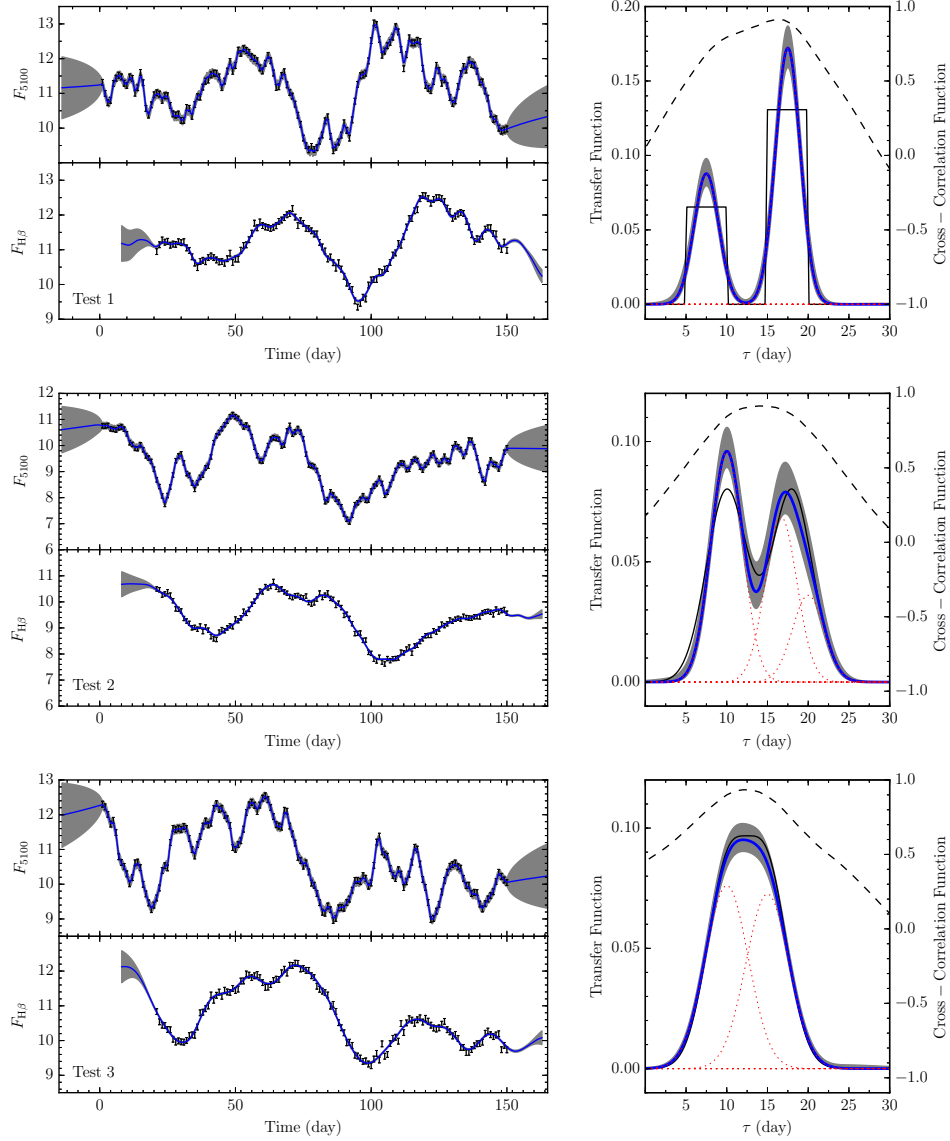


FIG. 3.— Three simulation tests of our approach. For each test, left panels: simulated light curves for 5100 Å continuum and H β emission line. Solid lines represent the recovered light curves and shaded areas represent their uncertainties. Right panel: The best recovered transfer function (in blue) compared with the input transfer function (in black). Shaded area represents the estimated uncertainties for the recovered transfer function. Red dotted lines represent the Gaussian functions that constitute the transfer function. Dashed line represents the interpolation cross-correlation function of the light curves.

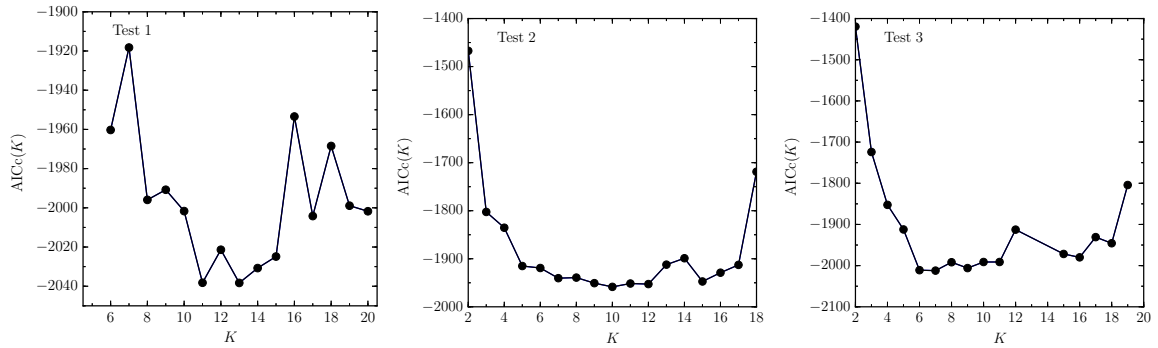


FIG. 4.— The AICc as a function of the number (K) of Gaussian functions for the three simulation tests in Figure 3. The AICc reaches a minimum at $K = 13$, 10, and 7, respectively.

information criteria (AIC; Akaike 1973), a measure of the relative quality of statistical models. The original form of AIC

is only valid asymptotically; Hurvich & Tsai (1989) proposed a correction to AIC for finite sample sizes (abbreviated to AICc). The AIC is defined by

$$\text{AIC} = 2m - 2 \log P(y|\hat{\sigma}, \hat{\tau}_d, \hat{\theta}), \quad (19)$$

where m is the number of parameters in the model and hat symbol denotes the best estimate for the corresponding parameter. The AICc is defined by

$$\text{AICc} = \text{AIC} + \frac{2m(m+1)}{n-m-1}, \quad (20)$$

where $n = N + M$ is total number of data points. The best choice of K is the one that minimizes the AICc.

We employ an MCMC method to determine the best estimates and uncertainties of free parameters. We use the Metropolis-Hastings algorithm to construct samples of free parameters from the posterior probability distribution. The Markov Chain is run 150,000 steps in total. The best estimates of free parameters are assigned the mean values of the samples and the associated uncertainties are assigned the 68.3% confidence levels (“1 σ ”) that enclose the mean values. The uncertainties of the final obtained transfer function in Equation (2) are determined by the error propagation formulas, under the best inferred K . Therefore, the uncertainty in the best inferred K is not included.

3. SIMULATION TESTS

In order to test our approach, we generate mock light curves of continuum and broad emission line with an assumption of transfer function, and then implement the above procedures to obtain the most probable estimate for the transfer function and compare it with the input one. As outlined by Rybicki & Press (1992), an unconstrained realization of mock light curves is simply a random series that has the covariance matrix $C = S + N$ with specified parameters σ and τ_d . We generate random numbers with the covariance matrix C using the Cholesky decomposition (see Zu et al. 2011). The Cholesky decomposition of a matrix is $C = MM^T$, where M is a lower triangular matrix with real and positive diagonal entries. If r is a series of Gaussian random numbers with a zero mean and unity dispersion, then $u = Mr$ has the covariance matrix of C , since $\langle uu^T \rangle = M \langle rr^T \rangle M^T = MM^T = C$. We first generate a mock continuum light curve and then convolve it with the adopted transfer function to produce a light curve of emission line.

3.1. Validity of the Method

We run three simulation tests by presuming the transfer functions to be composed of

1. two displaced top-hats,
2. two moderately mixed Gaussians (so that the transfer function is double-peaked), and
3. two severely mixed Gaussians,

respectively. The left panels of Figure 3 plot these three input transfer functions. Specifically, for the first test, the two displaced top-hats are (arbitrarily) configured to

$$\Psi(\tau) = \frac{1}{15} \times \begin{cases} 1 & \text{for } 5 < \tau < 10, \\ 2 & \text{for } 15 < \tau < 20, \\ 0 & \text{else,} \end{cases} \quad (21)$$

where 1/15 is the normalization factor. For the other two tests, the two Gaussians are (arbitrarily) configured to center at 10 and 18 days for moderately mixed case and 10 and 15 days for severely mixed case, with the same standard deviation of 2.5 days. The mean time lags for these three transfer functions are 14.2, 14.0, and 12.5 days, respectively, roughly corresponding to a 5100 Å luminosity of $\sim 10^{43}$ erg s⁻¹ according to the relation between BLR sizes and 5100 Å luminosities of AGNs (Bentz et al. 2013). For the DRW model of all the three tests, the parameter of damping timescale is set to $\tau_d = 100$ days, a typical value for a luminosity of 10^{43} erg s⁻¹ (Kelly et al. 2009; Zu et al. 2011; Li et al. 2013); the parameter of the variation amplitude is set to $\sigma_d = 0.6$ (in arbitrary units) such that the resulting variation amplitude is typically ~ 30 -50%. The time span of continuum monitoring is 150 days and the monitoring of emission line starts 20 days latter. The cadence is typically one day apart. The signal-to-noise ratio (S/N) is set to ~ 120 . It is worth stressing that the choice of these values is only for illustrative purposes and has no special meaning. The left panels of Figure 3 show the generated mock light curves of continuum and emission line for the three simulation tests.

Throughout the calculations, the range of time lag is set to (0-30) days. Since the best number of Gaussians is determined by the AICc, the final transfer function is insensitive to the adopted range of time lag, provided it is broad enough to enclose the time lag of the emission line. The obtained AICcs with the number of Gaussian functions K for the three tests are illustrated in Figure 4. The resulting optimal K is 13, 10, and 7, respectively. This means that the optimal K does not depend on the sampling cadence, but on the shape of the transfer function. The right panels of Figure 3 show the best recovered transfer functions with the optimal K . As can be seen, the structures in the transfer functions are successfully recovered and all the features in the light curves are also well reconstructed. However, we note that, in the first test, we fail to reproduce the top-hat shape because of the finite sampling and measurement errors of the light curves. Meanwhile, in the second test, although the recovered two peaks are marginally equal, the left peak seems slightly stronger than the right one. These tests suggest that, like all RM methods, the performance of the present approach depends on the data quality and the presence of strong variability features in the light curves, therefore, it may be unable to resolve very fine structures of the transfer function in some circumstances.

In the right panels of Figure 3, we also superimpose the interpolation cross-correlation function (CCF) of the light curves using the procedure of Gaskell & Peterson (1987). All the CCFs in the three tests are single peaked, indicating that CCF analysis hardly reveals more than the characteristic time lags of BLRs. In particular, the CCF in the first test is wide and peaks at $\tau = 17.5$ day. This is an appropriate choice for the time lag if one only concentrates on a single characteristic lag for the BLR, but clearly a single lag is not sufficient to describe the BLR in this case. In Appendix C, we show the time lag distributions from JAVELIN method for the above three simulation tests. JAVELIN presumes a top-hat transfer function and the time lag is assigned the mean lag of the top hat. We illustrate that while the present approach works fairly well in all the three tests, JAVELIN cannot appropriately recover the characteristic lag for the first test with a multimodal transfer function.

3.2. Dependence on Data Quality

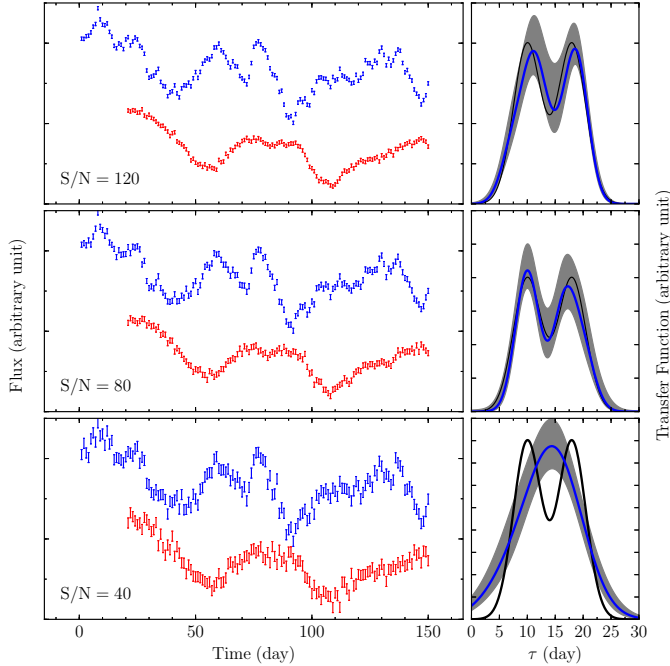


FIG. 5.— Tests of our approach with $S/N=120$, 80, and 40. The input transfer function is presumed to be two moderately mixed Gaussians (see 3.1 for details). For each test, left panel shows simulated light curves of 5100\AA continuum (in blue) and $H\beta$ line (in red), and right panel compares the best recovered (in blue) with the input (in black) transfer function. Shaded area represents the estimated uncertainties for the recovered transfer function.

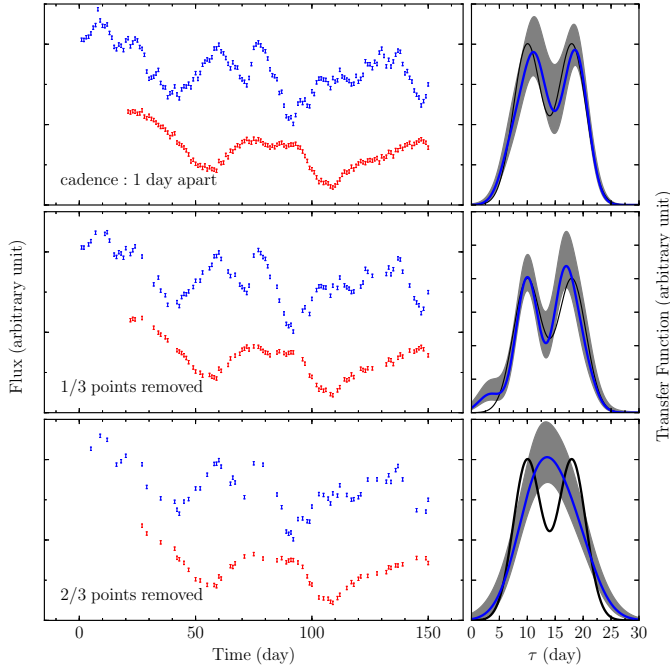


FIG. 6.— Same as Figure 5 but for different cadences. In the top panel, the cadence is 1 day apart. In the middle and bottom panels, we randomly remove about 1/3, and 2/3 points, respectively.

The above simulations show that our approach can generally well reproduce the input transfer function with optimal data quality. In this section, we test dependence of the obtained transfer function on data quality with different S/N s, sampling cadences, and time spans of mock light curves. We

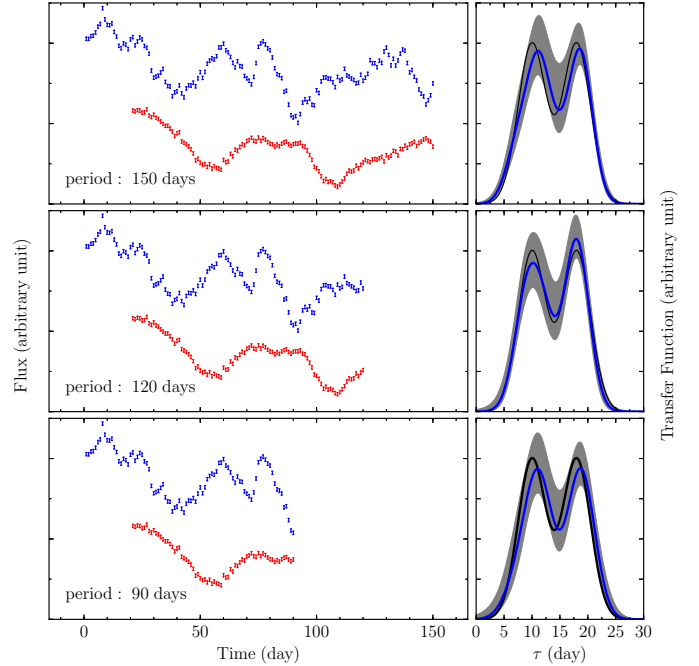


FIG. 7.— Same as Figure 5 but for monitoring periods of 150, 120, and 90 days.

only use the double-peaked transfer function for illustration, namely, the one used for the second simulation test in the preceding section. We fix the seed for the random number generator so that all the mock light curves in this section have the same variation pattern. This allows us to only focus on the desired factor that influences the obtained transfer function.

In Figure 5, we generate three sets of mock light curves with $S/N=120$, 80, and 40, respectively. As expected, when S/N is low enough, the weak variability signals in the light curves are overwhelmed by noises and the information of small structures in the transfer function is missing. Consequently, for the case of $S/N=40$ (bottom panels of Figure 5), we only obtain a single-peaked transfer function, which, however, has the same mean time lag with that of the input.

To check how the sampling rate affects the results, we respectively randomly remove about one-third and two-thirds points of the light curves with $S/N=120$ in Figure 5 and generate two new sets of mock datasets with degraded sampling rates. We show the light curves and the corresponding best recovered transfer function in Figure 6. Again, when the sampling cadence is poorer, more information on the fine structure of the transfer function is lost.

The default time span of the light curves is 150 days. In Figure 7, we reduce the time span to 120 and 90 days, by subtracting the last 30-day and 60-day section of the light curves with $S/N=120$ in Figure 5, respectively. The mean time lag of the input transfer function is 14 days, so that the overall time spans are still more than 6 times the mean lag (Welsh 1999). There is no surprise that the transfer function is well reproduced in all the three cases in Figure 7.

In summary, provided the time span is more than several times the mean time lag of the emission line, S/N and sampling cadence are more critical to recovering the transfer function. We stress again that the overall performance of the present approach depends on the presence of strong variation features in light curves and the specific structures of the trans-

fer function one desires to resolve. We therefore cannot specify more details about the data requirements for the present approach to faithfully recover the transfer function.

4. APPLICATION

We select three illustrative RM sources to show the feasibility of our approach: Arp 151, SBS 1116+583A, and Mrk 817. The first two objects were monitored by the Lick AGN monitoring project (LAMP⁶; Bentz et al. 2009; Walsh et al. 2009) and the last object was by Peterson et al. (1998). The RM data of Arp 151 was previously studied in great details by the maximum entropy method (Bentz et al. 2010), BLR dynamical modeling method (Brewer et al. 2011; Pancoast et al. 2014b), and RLI method (Skielboe et al. 2015). This allows us to further verify the validity of our approach. The transfer function of SBS 1116+583A derived by the RLI method of Skielboe et al. interestingly showed a bimodal distribution, meriting an analysis using our approach. The object Mrk 817 shows long-term secular trends in its light curves (Li et al. 2013), therefore adapted to illustrate the capability of our approach to cope with detrending.

To compare our results with those from CCF analysis, we define the mean time delay from the transfer function as (Rybicki & Kleyana 1994)

$$\tau_m = \frac{\int_{-\infty}^{\infty} \tau \Psi(\tau) d\tau}{\int_{-\infty}^{\infty} \Psi(\tau) d\tau} = \frac{\sum_k f_k \tau_k}{\sum_k f_k}. \quad (22)$$

The uncertainty of τ_m is calculated by the error propagation formulas.

4.1. Arp 151

For the sake of comparison with the previous results, we use the *B*-band photometric light curve of Arp 151 as a surrogate of the continuum as in Pancoast et al. (2014b) and Skielboe et al. (2015). The magnitudes are first converted into fluxes. Since the absolute unit of light curves are no longer important for RM analysis, we adopt an arbitrary zero-magnitude flux for the conversion. We set the range of time lag for solving the transfer function to be (0-10) days. The best number of Gaussian function is $K = 4$ according to the AICc criteria.

The top panels of Figure 8 present the reconstruction for the light curves of continuum and $H\beta$ line and the best recovered transfer function for Arp 151. The mean time lag from Equation (22) is $\tau_m = 3.33 \pm 0.26$ days, consistent with the previous results from CCF analysis $\tau_{CCF} = 4.08 \pm 0.60$ days (Bentz et al. 2009) and the JAVELIN method of Zu et al. (2011) $\tau_{JAV} = 3.68 \pm 0.36$ days (Grier et al. 2013a). The transfer function is mainly contributed by the second Gaussian component centered at $\tau = 3.33$ days.

In the top panel of Figure 9, we compare the transfer function derived in this work with those from RLI method (Skielboe et al. 2015) and from BLR dynamical method (Li et al. 2013). Our result well matches that from the dynamical modeling method, but differs from the RLI result, which has a plateau from zero to about 7 days. The shape of our obtained transfer function also coincides with that from the maximum entropy method (see Figure 1 in Bentz et al. 2010).

⁶ The spectroscopic data of LAMP project is publicly available from <http://www.physics.uci.edu/~barth/lamp.html>.

4.2. SBS 1116+583A

Same as for Arp 151, we use the *B*-band photometric light curve for this object. The range of time lag in the calculations is set to (0-10) days and the best number of Gaussian function is $K = 5$ according to the AICc criteria. The results are shown in middle panels of Figure 8. The obtained mean time lag is $\tau_m = 2.50 \pm 0.70$ days, which, again, is well consistent with the results based on CCF analysis $\tau_{CCF} = 2.38 \pm 0.58$ days (Bentz et al. 2009) and JAVELIN method $\tau_{JAV} = 2.46 \pm 0.93$ days (Grier et al. 2013a).

The middle panel of Figure 9 compares the derived transfer functions from various methods. The RLI method yields a bimodal transfer function with a response component around 2 days and an additional component around 8 days (Skielboe et al. 2015). However, both the transfer functions obtained in this work and from the dynamical modeling do not show the second component. An inspection of the reconstructed $H\beta$ light curves (see Figure 10 in Skielboe et al. 2015) indicates that our results better match the observations.

4.3. Mrk 817

Mrk 817 was monitored as long as five years in Peterson et al. (1998), but only during the intervening three years the $H\beta$ time lags were detected. We use the first-year section of the light curves with the $H\beta$ time lags detected (HJD 24,449,000–24,449,211). The CCF analysis by Peterson et al. (1998) yielded a time lag of $\tau_{CCF} = 20.1 \pm 4.4$ days. The range of time lag in our calculations is set (0-50) days and the best number of Gaussian functions is found to be $K = 4$. It is apparent from a simple visual inspection that the light curves of continuum and $H\beta$ line show different long-term trends, with that of the continuum fluxes decreasing more steeply. We therefore include the detrending procedure as described in Section 2.4, in which both the trends of continuum and $H\beta$ line are modeled by a linear polynomial. The results are plotted in the bottom panels of Figure 8. The transfer function peaks at around 17 days and bears large uncertainties due to poor data sampling. The resulting mean time lag also has a fairly large uncertainty $\tau_m = 16.7 \pm 8.3$ days. Nevertheless, all the variation features in the light curves are well reproduced.

This object was not ever analyzed by the RLI method or the maximum entropy method. The bottom panel of Figure 9 only shows a comparison of our result with that of the dynamical modeling method. Both the two results are generally consistent, although our result peaks at a slightly shorter time lag.

In our application to the above three RM objects, the transfer functions can be effectively modeled by a single Gaussian. As illustrated in Section 3.2, the time resolution of the obtained transfer function is determined by the data sampling and measurement noises of the observations. In a statistical sense based on the AICc criteria, the present solutions are the best ones that balance the trade-off between the goodness of fit and the complexity of our approach. Refining the sampling and signal-to-noise ratio can certainly provide more constraints on the fine structures in transfer functions (see Figure 2) if they are not intrinsically a simple single Gaussian.

5. DISCUSSIONS AND CONCLUSIONS

By extending the previous work of Rybicki & Press (1992) and Zu et al. (2011), we describe a non-parametric approach to determine the transfer function in RM. The basic princi-

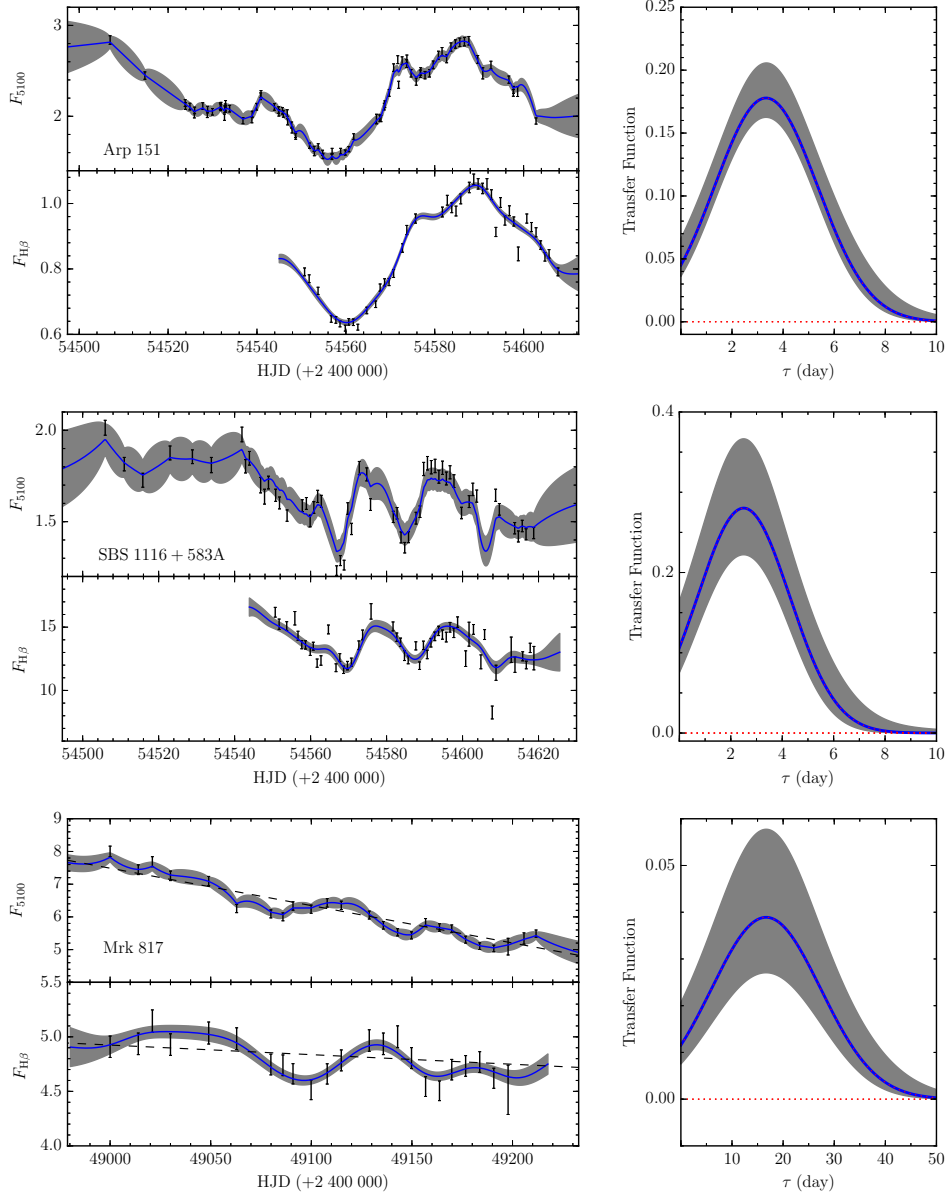


FIG. 8.— The best recovered transfer functions for Arp 151 (top), SBS 1116+583A (middle), and Mrk 817 (bottom). For each object, the left two panels show the light curves of continuum and $H\beta$ line (points with error bars), together with the best reconstructions (solid lines with shaded areas). The right panel show the best recovered transfer function with shaded area representing the uncertainties. Red dotted lines represent the Gaussian functions that constitute the transfer function. For Mrk 817, a detrending of long-term trend is included. The dashed lines in the left two panels show the best fit for the detrending.

ple that the transfer function can be expressed as a sum of a family of relatively displaced Gaussian functions enables us to largely obviate the need for the presumption of a specified transfer function or BLR model as in previous studies. Thus, this to some extent makes our approach model independent. In addition, following the framework of Zu et al. (2011), the inclusion of the statistical modeling of continuum variations as a DRW process allows us to naturally take into account the measurement errors and make use of the information in observation datasets as much as possible. Application to RM datasets illustrates the fidelity of our approach and its capability to deal with long-term, secular variations in light curves. In particular, our approach is apt at solving the multimodal transfer functions associated with multiple-component structures of BLRs (e.g., Hu et al. 2012). Not only of BLRs, our approach can also be applied to RM observations of dusty torus

in AGNs (e.g., Suganuma et al. 2006; Koshida et al. 2014).

Since we relax the presumption of a specified transfer function but let its shape be determined by the data, our approach can be regarded as a useful complementary constraint to the BLR dynamical modeling (Pancoast et al. 2011, 2014a; Li et al. 2013). Indeed, interpretation of the obtained transfer functions has to invoke physical BLR models. A combination of these two methods may help to remove the concern over the systematic errors in the dynamical modeling. On the other hand, compared with the RLI method and the maximum entropy method, we incorporate the statistical description for both the light curves of continuum and emission line; therefore, we take full advantage of the information in data and can estimate uncertainties for the obtained transfer function in a self-consistent manner.

We end with discussions on some improvements to be made

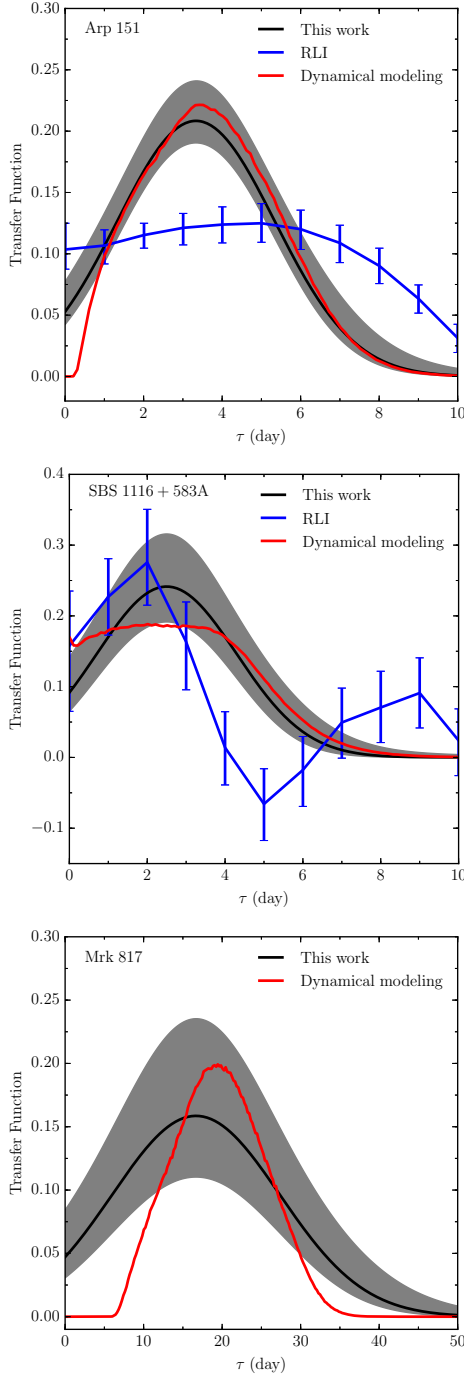


FIG. 9.— Comparisons of the transfer functions derived from different methods for Arp 151 (top), SBS 1116+583A (middle), and Mrk 817 (bottom). Black line with shaded areas is the transfer function from this work, blue line with error bars from the regularized linear inversion (RLI) method of Skielboe et al. (2015), and red line from the BLR dynamical modeling method of Li et al. (2013). Note that there is no RLI solution for Mrk 817. All the transfer functions are normalized on a common scale.

for our approach in the future.

- Throughout our calculations, we have by default assumed a linear response of emission line to the continuum so that the covariance functions of the light curves

can be analytically expressed by error function. To include non-linear response (Li et al. 2013), we can introduce a new parameter γ for the emission line fluxes as

$$f_i(t) = f_{i,\text{new}}^{1+\gamma}(t), \quad (23)$$

so that the new flux series $f_{i,\text{new}}(t)$ now linearly responds to the continuum.

- Since our approach is based on the statistical modeling of the temporal variations, it is not straightforward to directly include the velocity information. We can apply our approach to each velocity bin individually (e.g., Skielboe et al. 2015). In this case, any correlation information between velocity bins is neglected, thus, the obtained velocity-resolved transfer function may be sometimes noisy along the velocity direction. It merits a future development of a feasible scheme to self-consistently take into account the velocity information.
- We use the DRW process to describe the continuum variations, which is found to be sufficiently adequate for most of current AGN variability datasets (e.g., Kelly et al. 2009; MacLeod et al. 2010; Li et al. 2013; Zu et al. 2013). However, there is evidence that DRW process is no longer appropriate on short time scale of days (Mushotzky et al. 2011; Kasliwal et al. 2015; Kozłowski 2016). This impedes application of our approach in recovering very fine structures (on timescale of days) in the transfer function. Recently, Kelly et al. (2014) developed a flexible method that statistically describes the variability by a general continuous-time autoregressive moving average (CARMA) process. DRW process is a special case of CARMA process. In principle, our approach can also naturally include CARMA process, but this will make it highly computationally expensive. We therefore defer this to a future improvement with the parallelization of our approach on super-computer clusters.

We thank the two referees (astronomer and statistician) for useful suggestions that improved the manuscript. YRL thanks Ying Zu for useful discussions and Andreas Skielboe for providing the data of $H\beta$ light curve and their derived transfer function for SBS 1116+583A. This research is supported in part by the Strategic Priority Research Program - The Emergence of Cosmological Structures of the Chinese Academy of Sciences, Grant No. XDB09000000 and by NSFC grants NSFC-11173023, -11133006, -11233003, -11303026, -11573026, and -U1431228. This work has made use of data from the Lick AGN Monitoring Project public data release.

We developed a software package MICA (abbreviated from Multiple and Inhomogeneous Component Analysis) for the present approach, which is available upon request.

REFERENCES

- Bentz, M. C., Denney, K. D., Grier, C. J., et al. 2013, *ApJ*, 767, 149
 Bentz, M. C., Horne, K., Barth, A. J., et al. 2010, *ApJ*, 720, L46
 Bentz, M. C., Walsh, J. L., Barth, A. J., et al. 2009, *ApJ*, 705, 199
 Blandford, R. D., & McKee, C. F. 1982, *ApJ*, 255, 419
 Brewer, B. J., Treu, T., Pancoast, A., et al. 2011, *ApJ*, 733, L33
 Brotherton, M. S. 1996, *ApJS*, 102, 1
 Denney, K. D., Peterson, B. M., Pogge, R. W., et al. 2010, *ApJ*, 721, 715
 Du, P., Hu, C., Lu, K.-X., et al. 2015, *ApJ*, 806, 22
 Du, P., Lu, K.-X., Hu, C., et al. 2016, *ApJ*, 820, 27
 Gaskell, C. M., & Peterson, B. M. 1987, *ApJS*, 65, 1
 Grier, C. J., Martini, P., Watson, L. C., et al. 2013a, *ApJ*, 773, 90
 Grier, C. J., Peterson, B. M., Horne, K., et al. 2013b, *ApJ*, 764, 47
 Guerras, E., Mediavilla, E., Jimenez-Vicente, J., et al. 2013, *ApJ*, 764, 160
 Ho, L. C., & Kim, M. 2015, *ApJ*, 809, 123
 Hooten, M. B. and Hobbs, N. T. 2015, *Ecological Monographs*, 85, 3
 Horne, K. 1994, in *ASP Conf. Ser. 69, Reverberation Mapping of the Broad Line Region in Active Galactic Nuclei*, ed. P. M. Gondhalekar, K. Horne, & B. M. Peterson (San Francisco, CA: ASP), 23
 Horne, K., Korista, K. T., & Goad, M. R. 2003, *MNRAS*, 339, 367
 Hu, C., Wang, J.-M., Ho, L. C., et al. 2008, *ApJ*, 683, L115
 Hu, C., Wang, J.-M., Ho, L. C., et al. 2012, *ApJ*, 760, 126
 Hurvich, C. M. & Tsai, C.-L. 1989, *Biometrika*, 76, 297
 Kasliwal, V. P., Vogeley, M. S., & Richards, G. T. 2015, *MNRAS*, 451, 4328
 Kaspi, S., Maoz, D., Netzer, H., et al. 2005, *ApJ*, 629, 61
 Kaspi, S., Smith, P. S., Netzer, H., et al. 2000, *ApJ*, 533, 631
 Kelly, B. C., Bechtold, J., & Siemiginowska, A. 2009, *ApJ*, 698, 895
 Kelly, B. C., Becker, A. C., Sobolewska, M., Siemiginowska, A., & Uttley, P. 2014, *ApJ*, 788, 33
 Koshida, S., Minezaki, T., Yoshii, Y., et al. 2014, *ApJ*, 788, 159
 Kozłowski, S. 2016, *MNRAS*, in press (arXiv:1604.01773)
 Krolik, J. H., & Done, C. 1995, *ApJ*, 440, 166
 Li, Y.-R., Wang, J.-M., Ho, L. C., Du, P., & Bai, J.-M. 2013, *ApJ*, 779, 110
 MacLeod, C. L., Ivezić, Ž., Kochanek, C. S., et al. 2010, *ApJ*, 721, 1014
 Marshall, K., Ryle, W. T., & Miller, H. R. 2008, *ApJ*, 677, 880-883
 Maoz, D., Netzer, H., Mazeh, T., et al. 1991, *ApJ*, 367, 493
 Mushotzky, R. F., Edelson, R., Baumgartner, W., & Gandhi, P. 2011, *ApJ*, 743, L12
 Pancoast, A., Brewer, B. J., & Treu, T. 2011, *ApJ*, 730, 139
 Pancoast, A., Brewer, B. J., & Treu, T. 2014a, *MNRAS*, 445, 3055
 Pancoast, A., Brewer, B. J., Treu, T., et al. 2014b, *MNRAS*, 445, 3073
 Peterson, B. M. 1993, *PASP*, 105, 247
 Peterson, B. M. 2014, *Space Sci. Rev.*, 183, 253
 Peterson, B. M., Grier, C. J., Horne, K., et al. 2014, *ApJ*, 795, 149
 Peterson, B. M., Wanders, I., Bertram, R., et al. 1998, *ApJ*, 501, 82
 Rybicki, G. B., & Kleyana, J. T. 1994, in *ASP Conf. Ser. 69, Reverberation Mapping of the Broad-Line Region in Active Galactic Nuclei*, ed. P. M. Gondhalekar, K. Horne, & B. M. Peterson (San Francisco, CA: ASP), 85
 Rybicki, G. B., & Press, W. H. 1992, *ApJ*, 398, 169
 Shappee, B. J., Prieto, J. L., Grupe, D., et al. 2014, *ApJ*, 788, 48
 Sivia, D. S. & Skilling, J. 2006, *Data Analysis: A Bayesian Tutorial* (New York: Oxford Univ. Press)
 Skielboe, A., Pancoast, A., Treu, T., et al. 2015, *MNRAS*, 454, 144
 Sluse, D., Hutsemékers, D., Courbin, F., Meylan, G., & Wambsganss, J. 2012, *A&A*, 544, A62
 Suganuma, M., Yoshii, Y., Kobayashi, Y., et al. 2006, *ApJ*, 639, 46
 Sulentic, J. W., Marziani, P., Zwitter, T., Dultzin-Hacyan, D., & Calvani, M. 2000, *ApJ*, 545, L15
 Vestergaard, M., & Peterson, B. M. 2006, *ApJ*, 641, 689
 Walsh, J. L., Minezaki, T., Bentz, M. C., et al. 2009, *ApJS*, 185, 156
 Welsh, W. F. 1999, *PASP*, 111, 1347
 Zu, Y., Kochanek, C. S., Kozłowski, S., & Peterson, B. M. 2016, *ApJ*, 819, 122
 Zu, Y., Kochanek, C. S., Kozłowski, S., & Udalski, A. 2013, *ApJ*, 765, 106
 Zu, Y., Kochanek, C. S., & Peterson, B. M. 2011, *ApJ*, 735, 80

APPENDIX

A. COVARIANCE FUNCTIONS

In this appendix, we derive analytical expressions for S_{lc} and S_{ll} in Equations (4) and (5). In deriving S_{lc} , for the sake of clarity, we denote

$$S_{lc}(\Delta t) = \sum_k S_{lc}^k(\Delta t), \quad (\text{A1})$$

where S_{lc}^k represents the contribution to the covariance from the k -th Gaussian component. It is easy to show

$$\begin{aligned} S_{lc}^k(\Delta t) &= \sigma^2 f_k \left[\int_{-\infty}^{\Delta t} + \int_{\Delta t}^{\infty} \right] e^{-(\tau-\tau_k)^2/2\omega^2 - |\tau-\Delta t|/\tau_d} d\tau \\ &= \sqrt{\frac{\pi}{2}} \sigma^2 \omega f_k e^{\omega^2/2\tau_d^2} \left\{ e^{-\Delta T_1/\tau_d} \operatorname{erfc} \left[-\frac{1}{\sqrt{2}} \left(\frac{\Delta T_1}{\omega} - \frac{\omega}{\tau_d} \right) \right] + e^{\Delta T_1/\tau_d} \operatorname{erfc} \left[\frac{1}{\sqrt{2}} \left(\frac{\Delta T_1}{\omega} + \frac{\omega}{\tau_d} \right) \right] \right\}, \end{aligned} \quad (\text{A2})$$

where $\Delta T_1 = \Delta t - \tau_k$ and $\operatorname{erfc}(x)$ is the complementary error function.

Similarly, we denote

$$S_{ll}(\Delta t) = \sum_k \sum_m S_{ll}^{km}(\Delta t). \quad (\text{A3})$$

The covariance component S_{ll}^{km} is

$$S_{ll}^{km}(\Delta t) = \sigma^2 f_k f_m \int_{-\infty}^{\infty} \int_{-\infty}^{\infty} e^{-(\tau-\tau_k)^2/2\omega^2} e^{-(\tau'-\tau_m)^2/2\omega^2} e^{-|\Delta t - (\tau - \tau')|/\tau_d} d\tau' d\tau. \quad (\text{A4})$$

Introducing new variables $u = (\tau + \tau')$ and $v = (\tau - \tau')$, we have

$$S_{ll}^{km}(\Delta t) = \frac{1}{2} f_m f_k \sigma^2 \int_{-\infty}^{\infty} du \int_{-\infty}^{\infty} dv e^{-(u+v-2\tau_k)^2/8\omega^2} e^{-(u-v-2\tau_m)^2/8\omega^2} e^{-|\Delta t - v|/\tau_d}. \quad (\text{A5})$$

Note that

$$(u+v-2\tau_k)^2 + (u-v-2\tau_m)^2 = 2[u - (\tau_k + \tau_m)]^2 + 2[v - (\tau_k - \tau_m)]^2. \quad (\text{A6})$$

The above integral can be rewritten as

$$S_{ll}^{km}(\Delta t) = \frac{1}{2} f_m f_k \sigma^2 \int_{-\infty}^{\infty} du e^{-[u - (\tau_k + \tau_m)]^2/4\omega^2} \int_{-\infty}^{\infty} dv e^{-[v - (\tau_k - \tau_m)]^2/4\omega^2 - |\Delta t - v|/\tau_d}. \quad (\text{A7})$$

The first integration term is

$$\int_{-\infty}^{\infty} e^{-[u - (\tau_k + \tau_m)]^2/4\omega^2} du = 2\sqrt{\pi}\omega, \quad (\text{A8})$$

and the second integration term is

$$\left[\int_{-\infty}^{\Delta t} + \int_{\Delta t}^{\infty} \right] e^{-[v-(\tau_k-\tau_m)]^2/4\omega^2-|\Delta t-v|/\tau_d} dv = \sqrt{\pi}\omega e^{\omega^2/\tau_d^2} \left\{ e^{-\Delta T_2/\tau_d} \operatorname{erfc} \left[-\frac{\Delta T_2}{2\omega} + \frac{\omega}{\tau_d} \right] + e^{\Delta T_2/\tau_d} \operatorname{erfc} \left[\frac{\Delta T_2}{2\omega} + \frac{\omega}{\tau_d} \right] \right\}, \quad (\text{A9})$$

where $\Delta T_2 = \Delta t - (\tau_k - \tau_m)$. As a result, we arrive at

$$S_{ll}^{km}(\Delta t) = \pi\omega^2 f_m f_k \sigma^2 e^{\omega^2/\tau_d^2} \left\{ e^{-\Delta T_2/\tau_d} \operatorname{erfc} \left[-\frac{\Delta T_2}{2\omega} + \frac{\omega}{\tau_d} \right] + e^{\Delta T_2/\tau_d} \operatorname{erfc} \left[\frac{\Delta T_2}{2\omega} + \frac{\omega}{\tau_d} \right] \right\}. \quad (\text{A10})$$

B. ERROR FUNCTION

The error function is defined as

$$\operatorname{erf}(x) = \frac{2}{\sqrt{\pi}} \int_0^x e^{-t^2} dt. \quad (\text{B1})$$

The complementary error function is defined as

$$\operatorname{erfc}(x) = 1 - \operatorname{erf}(x) = \frac{2}{\sqrt{\pi}} \int_x^{\infty} e^{-t^2} dt. \quad (\text{B2})$$

It is trivial to show that the integrals

$$\int_{-\infty}^x e^{-t^2} dt = \frac{\sqrt{\pi}}{2} \operatorname{erfc}(-x), \quad (\text{B3})$$

and

$$\int e^{-(at^2+bt+c)} dt = -\frac{1}{2} \sqrt{\frac{\pi}{a}} e^{(b^2-4ac)/4a} \operatorname{erfc} \left(\sqrt{a}x + \frac{b}{2\sqrt{a}} \right) + \text{const}. \quad (\text{B4})$$

C. COMPARISON WITH JAVELIN

The present approach extends the work of Zu et al. (2011) by adopting a more flexible transfer function rather than a specified top-hat transfer function. As such, we can obtain more than the characteristic time lag and recover complicated structures in transfer function. In Figure 10, we run the public package JAVELIN developed by Zu et al. (2011) on the simulated light curves of the three tests in Section 3.1 and plot the obtained top-hat transfer functions and the distributions of the mean time lag of the top-hat. The recovered transfer functions from our approach and the input transfer functions are also superimposed for comparison. JAVELIN also employs an MCMC method (but with a different algorithm) to determine the best values of the free parameters. Again, we run the Markov Chain with 150,000 steps. The time-lag distribution for the first test is bimodal, with the two peaks at 15.53 ± 0.04 and 16.5 ± 0.1 days, respectively, and the overall mean lag of 16.2 ± 0.5 days. Here, the uncertainties are assigned the standard deviations of the distributions. The two peaks correspond to neither the mean lags of the input two top hats (7.5 and 17.5 days), nor the overall mean lag (14.2 days). The JAVELIN time lags for the second and third tests are 14.0 ± 0.2 and 12.5 ± 0.1 days, respectively, in agreement with the mean lags of the input transfer functions (14.0 and 12.5 days). However, for the second test, the time lag does not show the expected double-peak distribution. By contrast, the present approach works fairly well in all these three cases (see Figure 3), in terms of recovering both the shape of the transfer functions and the characteristic time lags. The present approach yields a mean time lag of 14.1 ± 0.5 , 14.1 ± 0.9 , and 12.4 ± 0.5 days for the three tests, respectively, generally consistent with the input values. Here, the uncertainties are calculated by applying the error propagation formulas on Equation (22). We attribute such discrepancies of JAVELIN to the too simplified top-hat transfer function adopted in the approach, which may encounter difficulties when the transfer function is multimodal and asymmetric.

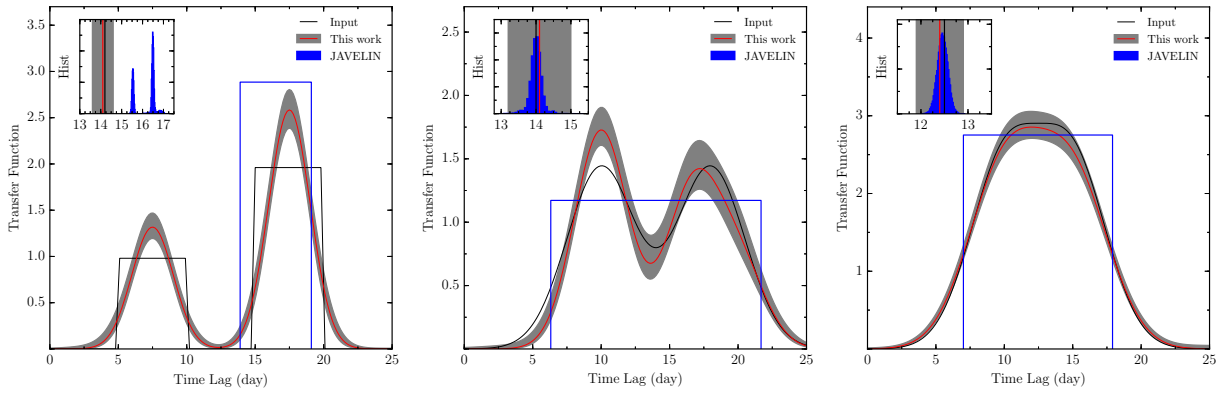


FIG. 10.— Comparison of the best recovered transfer functions from our approach (red lines with shaded areas) with JAVELIN (blue lines) for the simulated light curves of the three tests in Figure 3. Black lines show the input transfer functions. The transfer functions are adjusted to a common scale. The inset panels highlight the histograms of the mean time lags of the top hat from JAVELIN, along with the mean time lags of the transfer functions from the input and our approach, indicated by black vertical lines and red vertical lines with shaded areas, respectively.